GEOLOGICA CARPATHICA, DECEMBER 2018, 69, 6, 558–572 doi: 10.1515/geoca-2018-0033

In-situ U–Th–Pb geochronometry with submicron-scale resolution: low-voltage electron-beam dating of complexly zoned polygenetic uraninite microcrystals

MICHAEL WAITZINGER✉ and FRITZ FINGER

Department of Chemistry and Physics of Materials, University of Salzburg, Jakob-Haringer-Strasse 2a, A-5020 Salzburg, Austria;
✉Michael.Waitzinger@sbg.ac.at

(Manuscript received August 2, 2018; accepted in revised form November 5, 2018)

Abstract: Complexly zoned microcrystals of uraninite were encountered in orthogneiss from the central Tauern Window in Austria (K1 gneiss, Felbertal scheelite mine) and analysed in-situ for U, Th and Pb with state-of-the-art FE-SEM/EDX techniques. A three times finer spatial resolution was achieved using an acceleration voltage of 8 kV, compared to the classic 15–20 kV set-up of U–Th–total Pb electron microprobe dating. The lower voltage allows a spheroid of material with a diameter of only 0.3 µm to be selectively analysed. Careful tests on three uraninite reference materials show that the low-voltage method yields sufficient precision and accuracy for U–Th–total Pb uraninite dating, with errors on individual spot ages in the order of 10–30 Ma. By means of this innovative analysis technique, small-scale age zoning patterns could be resolved and dated in the uraninite microcrystals from the orthogneiss. Based on microstructures observed in backscattered electron images we interpret that an older uraninite generation in the rock, with a late Permian formation age (~260 Ma), was recycled two times through a coupled dissolution–reprecipitation process at ~210 Ma and at ~30 Ma. The younger dissolution–reprecipitation phase at ~30 Ma coincides with the Alpine regional metamorphism (lower amphibolite facies). The two older ages (~210 Ma and ~260 Ma) have been previously recognized in rocks from the Tauern Window by uraninite dating, but it is the first time here that both are recorded in the same rock and even the same uraninite grain. The present study shows that recrystallized accessory uraninite can provide a sensitive geological "hard disk" where several discrete thermal events of an area are stored. In addition, our work attests that the mineral uraninite has an unexpected geochronological robustness, even on the microcrystal scale.

Keywords: uraninite, high-resolution in-situ U–Th–Pb dating, K1 gneiss, Tauern Window.

Introduction

U–Th–Pb geochronometry is undoubtedly one of the most important analytical tools that are used in the Earth Sciences. Since its beginnings (Holmes 1911), the field has continuously improved with regard to better precision, more sophisticated analytical techniques, lesser sample material, and in-situ dating with high spatial resolution (e.g., Krogh 1982; Kober 1986; Williams 1998; Davis et al. 2003; Foster et al. 2004; Mattinson 2005; Amelin & Davis 2006; Frei & Gerdes 2009; Schoene et al. 2010; Schaltegger et al. 2015). Apart from zircon and monazite, which are the dominant targets for U–Th–Pb dating at present, minerals like titanite, rutile, xenotime, columbite, uraninite, thorite, and several others have been used.

The common method for U–Th–Pb age dating is based on isotopic measurements with mass spectrometers (TIMS, SIMS, SHRIMP, Laser-ICP-MS). An alternative is the determination of total Pb contents in Th- and U-rich minerals using electron beam methods (Parslow et al. 1985; Bowles 1990; Suzuki et al. 1991; Montel et al. 1996, 2017; Williams & Jercinovic 2002). The latter method has the advantage of a high spatial analytical resolution (typically 1–2 µm in the traditional setups), thus enabling the targeting of small crystals as well as the detailed study of age-zoned crystals. Furthermore, chemical data is collected simultaneously with the age information, which is helpful for many petrogenetic issues. Electron beam analyses can be performed on minerals in thin section, and, thus, the age dates can be directly related to mineral textures. Disadvantages of U–Th–total-Pb electron-beam dating include its poorer precision and accuracy in the measured ages, and poorer control on determining the possible effects of Pb loss or common Pb presence. Electron beam dating is currently mainly applied to monazite, although successful studies with other U–Th-bearing minerals have been made as well, for instance with zircon (Geisler & Schleicher 2000), xenotime (Bernhard et al. 1998), zirconolite (Tropper et al. 2007), thorianite, thorite, huttonite and uraninite (Förster 1999; Santosh et al. 2003; Cocherie & Legendre 2007; Naemura et al. 2009; Yokoyama et al. 2010; Cross et al. 2011; Votyakov et al. 2013; Allaz et al. 2015).

This work is focused on two examples of complexly zoned microcrystals of uraninite that were encountered in an orthogneiss from the Tauern Window in the Eastern Alps. In a previous study (Finger et al. 2017), a significant intra-crystal variation of U/Pb ratios was observed in these zoned grains, pointing to a polygenetic origin. Notably, other uraninite microcrystals in this gneiss showed a homogeneous intra-crystal

U/Pb distribution with an either Permian or Paleogene total Pb age. The origin and geological significance of the two age-zoned grains thus constituted an interesting problem for further research.

The investigation of small-scale compositional heterogeneities in micron-sized uraninite grains requires a particularly high spatial analytical resolution. Using FE-SEM/EDX techniques and a low-voltage (8 kV) electron beam, crystal volumes with an approximately 0.3 µm diameter can be selectively analysed. This low-voltage method is applied here for the first time to the U–Th–Pb dating of minerals. Therefore, a significant part of this paper will be devoted to methodology.

Methodology

General remarks

Using the standard electron microprobe setup with a 15–20 kV acceleration voltage, electron beam dating excites a spheroid-shaped volume with 1–3 µm diameter in the targeted minerals (Jercinovic et al. 2012). The exact size and geometry of the excitation volume depends on mineral density and composition. This 1–3 µm resolution is too coarse for the study of micron-sized crystals. A significantly better spatial resolution of electron beam dating can be achieved by lowering the acceleration voltage. For instance, at an acceleration voltage of 8 kV, and a beam width of 100 nm, the excitation volume in uraninite should theoretically be only ~0.3 µm in diameter, compared to ~0.8 µm at 15 kV (Fig. 1). Low-voltage (i.e., 8 kV) electron beam measurements on uraninite thus permit U–Th–total Pb dating at a three times finer spatial resolution, but the intensity of the generated X-ray signal that is needed for chemical analysis is much weaker in such conditions. Fortunately, special large-area EDX detectors have become available over the past ten years that are more sensitive and with much better counting statistics than previous generation EDX detectors. In addition, new field emission (FE) cathodes are a great advantage for high-resolution analysis, as they can produce a small coherent beam with a high current density.

Analytical setup

In this study, uraninite analyses were carried out on polished and carbon-coated rock thin-sections using a Zeiss ULTRA-PLUS scanning electron microscope (SEM) equipped with a field emission (FE) cathode. Uniform electron beam conditions were used for quantitative analysis involving an accelerating voltage of 8 kV, 2 nA beam current and 100 nm beam width. EDX analysis was performed with the large-area (50 mm^2) silicon drift detector X-MAX 50 from Oxford Instruments. A full spectrum range from 0 to 10 keV was recorded with 2048 channels and a resolution of 5 eV per channel. Concentrations of U, Th and Pb were derived from count rates obtained on the Mα lines using Oxford INCAEnergy software. Background, matrix and fluorescence effects, as well as line overlaps, are automatically computed and corrected by this software. Quantification of concentrations is based on intensity values taken from the Oxford INCAEnergy internal standard data bank (Table 1) and a 180 s calibration measurement on a Si wafer before every analytical session.

For quantitative uraninite measurements, the following element list was used: Al_2O_3, SiO_2, P_2O_5, SO_3, CaO, TiO_2, FeO, Y_2O_3, La_2O_3, Ce_2O_3, PbO, ThO_2, and UO_2. Some of these elements are uncommon in uraninite but were included to identify contamination from inclusions or boundary minerals. Oxygen was generally calculated using the stoichiometry based on the cations and not from the measured oxygen signal, as the latter is difficult to calibrate accurately and is oversensitive to surface contamination and oxidization. However, the oxygen (and carbon) peak intensities were routinely checked for anomalies in order to recognize any local alteration involving oxidization, hydration or carbonation. Furthermore, every spectrum was checked for the presence of any additional peak not included in the quantitative analysis.

The challenge for U–Th–total Pb dating is to analyse these three elements with such precision that permits sufficiently precise age dates to be calculated. When analysing uraninite under the aforementioned beam conditions, the Oxford X-MAX 50 acquires a total count rate of ~2*10^6 counts within

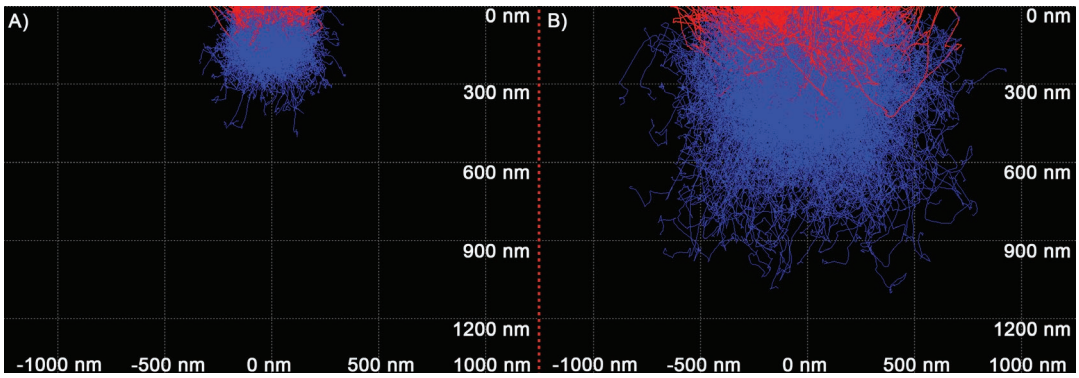

Fig. 1. Spatial resolution of electron beam dating of uraninite illustrated by Monte Carlo simulations of electron scattering at 8 kV (**A**) and 15 kV (**B**). Assumed beam width is 100 nm. Red: backscattered electrons. Used software: CASINO, Drouin et al. (2007).

Table 1: SEM/EDX set-up used in this study for low-voltage (8 kV) uraninite analysis. In columns 4–5, detection limits and typical errors (1 σ) are listed for selected elements, at 3 min counting time (120 s live time). The given detection limits and errors have been calculated by the INCAEnergy software based on measurements on synthetic uraninite and the Mitterberg uraninite standard, respectively. Blank values refer to pure UO_2.

Element	Line	Calibration standard	Detection limit 120s*	Typical error 120s*	Blank correction
Al	K_SERIES	Al_2O_3	0.06	0.02	
Si	K_SERIES	SiO_2	0.15	0.05	
P	K_SERIES	GaP	0.09	0.03	
S	K_SERIES	FeS_2	0.06	0.02	
Ca	K_SERIES	Wollastonite	0.18	0.06	
Ti	K_SERIES	Ti	0.36	0.12	
Fe	L_SERIES	Fe	0.99	0.33	
Y	L_SERIES	Y	0.36	0.12	
Zr	L_SERIES	Zr	0.33	0.11	
La	L_SERIES	LaB_6	1.29	0.43	
Ce	L_SERIES	CeO_2	1.26	0.42	
Pb	M_SERIES	PbF_2	0.21	0.12	−0.16±0.06
Th	M_SERIES	ThO_2	0.75	0.25	−0.83±0.37
U	M_SERIES	U		0.40	

c. 3 minutes (120 s live time). This results in an analytical precision of approximately ±0.4 wt. % (1σ) for U, while Pb can be analysed at a detection limit of ~0.2 wt. %. Thorium and other minor elements, like Si, Ca, Ce, and Y, that are occasionally reported in uraninite (Allaz et al. 2015; Alexandre et al. 2016), can be analysed at detection limits of 0.1–1.3 wt. % (Table 1). We are aware that these detection limits are far beyond the sensitivity of WDX microprobe analysis, but believe that this creates no essential problem for uraninite dating. For instance, a 90 Ma old uraninite crystal (see Table 2) contains ~1 wt. % radiogenic Pb, which is well within the measurable range. Using an 8 kV/2 nA beam and a counting time of 3 minutes, the analytical uncertainty for Pb in uraninite is typically ~0.1 wt. %, which corresponds to an error in the order of 20 Ma (1 σ) for a single spot age. Even when the counting time per spot is reduced to one minute (30 s live time), reasonable age errors in the order of 20–30 Ma can still be obtained. Increasing the counting time per analysis spot to five minutes or more improves detection limits and precision and could be favourable for very young, Pb-poor uraninite. However, we must be aware that this increases the risk for beam drift impeding the desired spatial resolution, as well as the risk for beam damage effects.

A sufficient analytical precision is a prerequisite for U–Th–total Pb dating. However, the successful application of any analytical method is also dependent on the accuracy of the element analysis, in particular the determination of Pb. As shown by Pyle et al. (2002) and Jercinovic et al. (2005, 2012) for electron-microprobe-based U–Th–total Pb monazite dating, there are many possible pitfalls that can superimpose a systematic analytical error on the Pb determination; the most important of these refer to background and interference correction problems.

For uraninite dating, these analytical perils are less severe because Pb contents are relatively high in uraninite; for example, they are commonly an order of magnitude higher than in monazite and generally reach a major element concentration. Nevertheless, we have carried out several of the recommended tests (Jercinovic et al. 2012) in order to assess the reliability of our data (see next sections).

Testing the calibration with synthetic uraninite and other mineral standards

A synthetic UO_2 crystal with 99.9 % purity was measured to control and validate the so-called "standardless" calibration provided by the Oxford INCAEnergy software. The obtained UO_2 concentrations were between 98 and 102 wt. % (mean 99.6±0.8 wt. %, n=8), confirming that UO_2 concentrations can be sufficiently accurately determined at 8 kV conditions with the internal INCAEnergy calibration. For a synthetic ThO_2 crystal, we obtained a value of 101.10±0.8 wt. % ThO_2, which is a little too high, but the effects of this ~1 wt. % standardization inaccuracy on the age dating results are negligible. Measurements on various Pb minerals also reproduced the recommended values within 3 % deviation. Even for difficult-to-analyse Pb minerals such as galena (line overlap of S Kα and Pb Mα) acceptable values were obtained (e.g., 87.3 wt. % Pb vs. expected 86.6 wt. % for stoichiometric galena).

Repeated measurements on the nominally Pb-free UO_2 showed that the computation of the Pb by INCAEnergy resulted in a small but systematic blank value of −0.16± 0.06 wt. % PbO. This blank value was externally corrected for all uraninite analyses, weighted by the individually measured UO_2. The validity of this procedure was independently assessed by measurements on uraninite reference materials (see below). The uncertainty of the blank value determination (±0.06 wt. %) was incorporated in the total Pb error and the age error.

Appreciable inaccuracies in the automatic INCAEnergy background and interference correction for uraninite were also encountered in the case of Th. A blank test on pure UO_2 gave a slightly negative ThO_2 content of −0.83±0.37 wt. % (see Table 1), probably because the peak interference of U Mα on Th Mα was slightly overcorrected. Consequently, an external Th correction was applied for every uraninite analysis, weighted according to the individual UO_2 content. This empirical Th correction is certainly not ideal, but the problem with accurately determining the Th will generally have only a minor influence on the final uraninite age calculations. For instance, 1 wt. % more or less Th alters the calculated age by less than 1 Ma. Nevertheless, it could be argued that the imprecise Th data may perhaps have some effect on the peak interference correction for Pb, as there is a small Th line close to the Pb Mα position. Indeed, Th and Y interference effects create a well-known analytical problem for electron-beam monazite dating (Scherrer et al. 2000). However, for uraninite dating, this will, in general, be negligible, owing to

the commonly high radiogenic Pb concentrations. The exception would perhaps be when analysing young, Pb-poor uraninite or very Th- and Y-rich uraninite.

Measurements on uraninite reference materials

Three in-house uraninite reference materials were measured for control and to serve as sensitive secondary Pb standards for comparison with the obtained U–Th–total Pb ages. The first reference material is magmatic uraninite from the Kirchberg granite, Erzgebirge, Germany, previously dated at 326±4 Ma (Förster 1999) and 330±5 Ma (Kempe 2003) by EPMA. The second is hydrothermal uraninite from Mitterberg, Austria, dated at 90±5 Ma by a concordant U^{238}–Pb^{206} TIMS age (Paar & Köppel 1978). The third reference material is magmatic uraninite from the Königshain granite, Erzgebirge, dated by EPMA at 328.6±1.9 Ma (Förster et al. 2012).

Our low-voltage measurements reproduce the published geochronological dates in all three cases surprisingly well (Fig. 2), showing that the Pb analyses are sufficiently accurate. Individual spot ages for the Mitterberg uraninite ranged between 85±11 Ma and 102±11 Ma, with a calculated mean age of 90.7±6.2 Ma (95 % confidence level, n=12). For the Kirchberg uraninite, individual ages ranged between 320±12 and 335±12 Ma, with a mean of 327.3±6.8 Ma (95 % confidence level, n=12). For the Königshain uraninite, we obtained an age range of 320–331 Ma and a mean age of 325.9±8.7 Ma (95 % confidence level, n=8). The low analytical totals of the Königshain uraninite (Table 2) result from additional REE amounts, which can be qualitatively recognized in the EDX spectra (Fig 3), but were unquantifiable within the used analytical setup. According to electron microprobe data (Förster 1999; Förster et al. 2012), the Königshain uraninite has a total REE content of 4–8 wt. %.

The reproduction of the published age for the Königshain reference material shows that our analytical setup also provides sufficiently accurate Pb values for Y-, REE-, and Th-rich uraninite, implying that the Pb background and interference corrections of the INCAEnergy software are good. The latter is independently supported by blank tests made for Pb-free synthethic ThO_2 and YPO_4, which yield a zero concentration result for Pb. In addition, Pb blank testing was done on Pb-free quartz and pyrite, and the measured Pb values were also close to zero.

Finally, a test for beam damage and charging effects was made using uraninite from Mitterberg. Repeated 30 s measurements on the same standard point yielded constant U count rates over a five-minute observation time, with a standard deviation not greater than the counting statistics of the instrument. The specimen current also remained constant within these five minutes of exposure time, suggesting that beam damage and charging effects play no or only a minor role at the given beam energy dose.

Table 2: Chemical data (wt. %) for the in-house uraninite reference materials Kirchberg, Mitterberg and Königshain. Single point ages and errors (1 σ) were calculated based on the measured U, Th and Pb concentrations, using the algorithm of Săbău (2012). Counting time per analysis is c. 5 minutes (180 s live time). The age errors always include the analytical uncertainties in the Pb and U determination as well as the error for the performed Pb blank correction. Mean ages (95 % confidence level) were calculated using the program ISOPLOT of Ludwig (2003).

Sample	SiO_2	CaO	Y_2O_3	PbO	ThO_2	UO_2	Total	Age	Error
Kirchberg	0.22	<0.11	<0.38	4.32	1.39	93.74	99.67	335	12
Kirchberg	<0.15	<0.11	<0.38	4.29	1.26	94.61	100.17	330	12
Kirchberg	0.21	<0.11	<0.38	4.21	1.21	94.43	100.05	325	12
Kirchberg	<0.15	<0.11	<0.38	4.28	1.42	94.32	100.01	330	12
Kirchberg	0.26	<0.11	<0.35	4.27	1.10	94.19	99.81	330	12
Kirchberg	0.33	<0.11	<0.38	4.11	1.02	92.20	97.66	325	12
Kirchberg	0.40	<0.11	<0.38	4.06	1.01	92.46	97.92	320	12
Kirchberg	0.42	<0.11	<0.35	4.24	1.05	94.54	100.25	327	12
Kirchberg	0.32	<0.11	<0.35	4.23	1.10	93.96	99.60	328	12
Kirchberg	0.37	<0.11	<0.35	4.25	0.95	93.95	99.51	329	12
Kirchberg	0.35	<0.11	<0.35	4.14	1.11	94.05	99.66	321	12
Kirchberg	0.31	<0.11	<0.35	4.16	1.00	92.69	98.17	327	12
Average age (95 % c.l.)								***327.3***	***6.8***
Mitterberg	0.41	0.41	0.77	1.29	<0.48	94.06	97.22	102	11
Mitterberg	0.37	0.47	0.81	1.12	<0.48	94.82	97.87	89	11
Mitterberg	0.34	0.53	0.83	1.16	<0.54	97.89	101.06	89	11
Mitterberg	0.32	0.58	1.49	1.08	<0.48	95.11	98.86	85	11
Mitterberg	0.36	0.44	1.42	1.16	<0.53	96.34	100.04	90	11
Mitterberg	0.33	0.48	1.31	1.09	<0.48	95.98	99.48	85	11
Mitterberg	0.20	0.67	1.11	1.12	<0.50	96.30	99.99	87	11
Mitterberg	0.26	0.65	0.89	1.18	<0.50	94.11	97.59	93	11
Mitterberg	0.25	0.66	0.79	1.24	<0.48	96.37	99.82	96	11
Mitterberg	0.30	0.44	0.85	1.17	<0.50	95.88	98.93	91	11
Mitterberg	0.27	0.63	0.64	1.18	<0.48	97.25	100.24	91	11
Mitterberg	0.31	0.49	0.61	1.16	<0.48	97.22	100.06	89	11
Average age (95 % c.l.)								***90.7***	***6.2***
Königshain	0.57	<0.14	4.23	3.56	7.09	76.90	92.34	329	13
Königshain	0.54	<0.14	4.31	3.56	6.58	76.51	91.49	331	13
Königshain	0.64	<0.14	4.66	3.54	6.90	77.25	92.99	326	13
Königshain	0.52	<0.14	4.36	3.48	6.57	75.99	90.91	326	13
Königshain	0.69	<0.12	3.48	3.58	7.49	79.47	94.72	320	12
Königshain	0.67	<0.12	3.77	3.61	6.81	79.49	94.35	324	12
Königshain	0.56	<0.12	3.20	3.63	7.61	80.08	95.08	322	12
Königshain	0.73	<0.12	3.55	3.60	7.60	77.42	92.90	330	13
Average age (95 % c.l.)								***325.9***	***8.7***

Testing the spatial resolution of low-voltage electron beam dating

The Mitterberg uraninite carries several small inclusions and veins of gold (Fig. 4). We recorded detailed chemical profiles across the uraninite-gold grain boundaries

at 8, 10, and 15 kV, using a step width of 0.1 µm, to empirically determine the lateral analytical resolution and the size of the excitation volume, respectively. Results are shown in Figure 5. At 15 kV, we note a ~1 µm wide transition zone, where the electron beam has excited both minerals, simultaneously producing signals for Au and U. The width of this transition zone is reduced from ~1 µm to ~0.6 µm at 10 kV and to ~0.3 µm at 8 kV, demonstrating that the spatial resolution of U–Th–Pb uraninite dating is about three times better at 8 kV than at 15 kV.

Recommended analysis strategy for uraninite dating

The suitability of monazite for electron beam U–Th–Pb dating has been highlighted many times (no significant Pb loss, little common Pb), but the potential of using uraninite as a geochronometer is still insufficiently investigated. There is agreement that the amount of common Pb in uraninite is generally strongly subordinate compared to the vast amounts of radiogenically produced Pb (e.g., Kotzer & Kyser 1993; Fayek et al. 2002; Chipley et al. 2007). Thus, the common Pb effect on a total Pb uraninite age date will be negligibly low in most cases.

However, problems with Pb loss can be serious. Investigations made on hydrothermally overprinted U deposits show that primary uraninite can lose Pb and become variably "rejuvenated" by interaction with fluids (Fayek et al. 2002; Alexandre & Kyser 2005; Decrée et al. 2011). Moreover, U gain can also occur when uraninite undergoes hydrothermal alteration (Kempe 2003). The key point here is to find

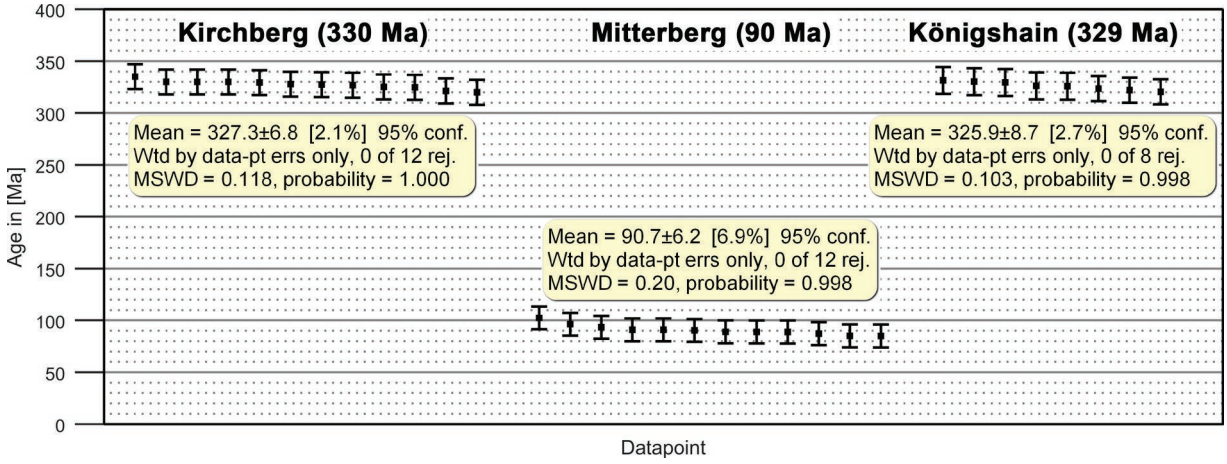

Fig. 2. Geochronological dates obtained for three uraninite reference materials using a low voltage electron beam (8 kV). Age data are sorted from oldest to youngest left to right. Recording time is c. 5 minutes (180 s live time) per analysis point. Mean ages, errors and statistical parameters were calculated with the program ISOPLOT (Ludwig 2003).

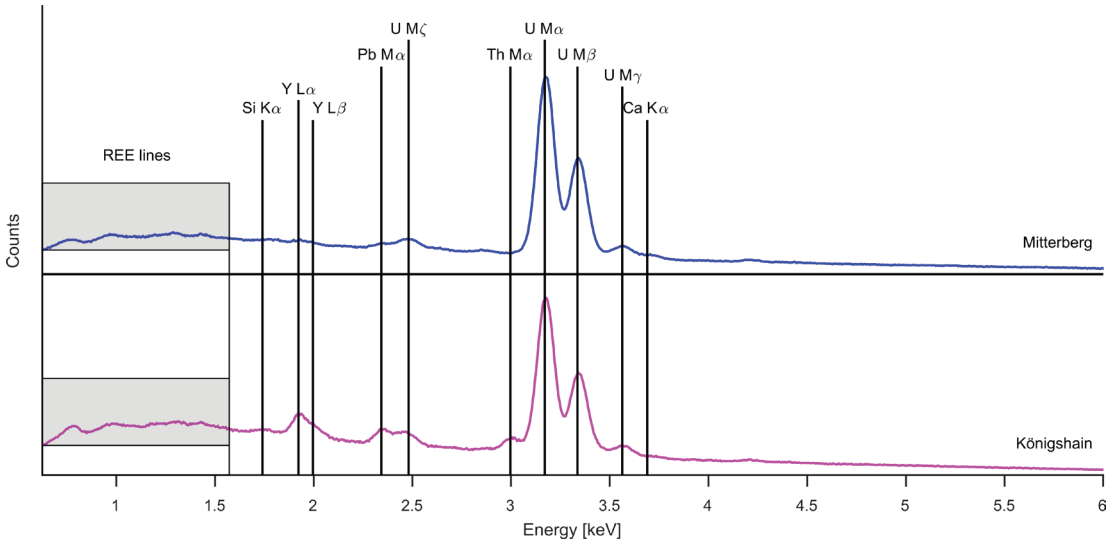

Fig. 3. Examples of EDX spectra (8 kV, 2 nA) for almost pure uraninite with ~1 wt. % PbO (Mitterberg), and Th, Y and REE bearing uraninite with ~3.5 % PbO (Königshain).

and develop an effective analytical strategy that enables us to determine whether the Th–U–Pb system of a given crystal (or crystal domain) is chemically disturbed or not (thermodynamically a closed or open system). Measuring the U–Th–Pb concentrations within single crystals at a high spatial resolution, for example, along a profile, could provide such a strategy. A constancy of ages would strongly suggest that the U–Th–Pb system is undisturbed, whereas a disturbed system will exhibit irregular U–Th–Pb distributions and inconsistent ages (Kempe 2003). If several adjacent spot ages along a profile are identical within the analytical error, they can be statistically averaged to produce a domain age. If all spot analyses in a grain are identical within error, they can be averaged to give a single grain age.

The case study: complexly zoned uraninite microcrystals in orthogneiss

Geological background and sample petrography

The Tauern Window exposes the deepest tectonic units of the Eastern Alps (Fig. 6). It contains crustal rocks of the European plate that were overridden by various nappes derived from the southern Adriatic plate during the Alpine orogeny (see Schmid et al. 2004, 2013 for review). As a consequence of this tectonic burial, the Tauern Window experienced upper greenschist to middle amphibolite facies regional metamorphism in the late Paleogene, at c. 30 Ma. This phase of regional metamorphism has been well constrained by various geochronological studies, including K–Ar and Ar/Ar mica and hornblende dating, Sm–Nd garnet dating (data compilation in Pestal et al. 2009) and U–Pb allanite dating (Cliff et al. 2015).

Approximately half of the Tauern Window complex comprises the so-called Penninic Units (Fig. 6) of Mesozoic sedimentary and volcanic rocks, including obducted Jurassic–Cretaceous ophiolites (Frasl & Frank 1966). An older, pre-Mesozoic basement (Subpenninic Units in Fig. 6) of Early Paleozoic, island arc-type crust was variably metamorphosed during the Variscan period (Habach Complex and Altkristallin in Fig. 6), and intruded by large volumes of Variscan granitoids, now the so-called Central Gneisses. The pre-Alpine geochronology of the Tauern Window is based mainly on Carboniferous to Permian zircon dates from the Variscan granitoids (Eichhorn et al. 2000; Vesela et al. 2012) and Cambro–Ordovician to Devonian zircon dates from the older arc-type crust (Eichhorn et al. 1995; Kebede et al. 2005). Carboniferous (Variscan) metamorphism is recorded through garnet and monazite ages (Von Quadt 1992; Finger et al. 2016).

Microcrystals of accessory uraninite have recently been found in several of the Central Gneisses of the Tauern Window. They have different formation ages (Finger et al. 2017). The youngest generation of uraninite microcrystals formed during the Alpine orogeny in the Paleogene at ~30 Ma. A Permian (~265 Ma) generation of uraninite microcrystals has been identified in the Central Gneiss types with a lower Carboniferous intrusion age (K1 gneiss and Felbertauern Augengneiss). Triassic (~215 Ma) uraninite microcrystals were found in the Central Gneisses with Permian intrusion ages (Granatspitz and Reichenspitz gneiss). The pre-regional metamorphic uraninite microcrystals are interpreted as dating

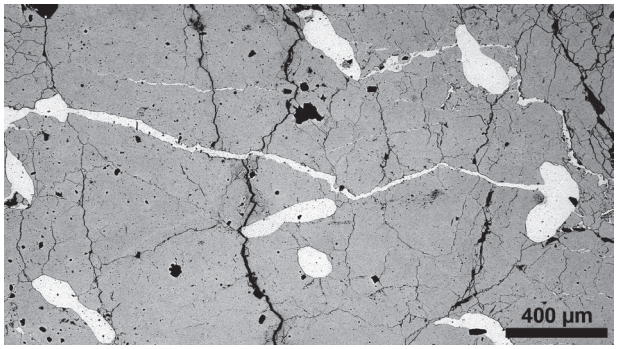

Fig. 4. Intergrowths of uraninite (grey) and gold (bright) in the Mitterberg sample (backscattered electron image).

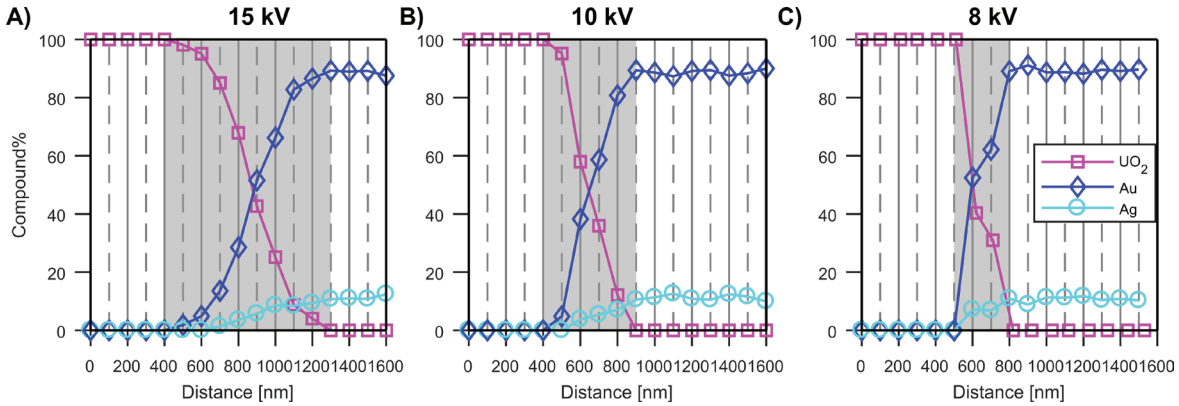

Fig. 5. Profiles across a uraninite-gold boundary (uraninite left, gold right) with a stepwidth of 0.1 µm, showing the spatial resolution of electron beam excitation at 15, 10 and 8 kV acceleration voltage (see text for further explanation). The gold occurs in solid solution with ~10 % silver.

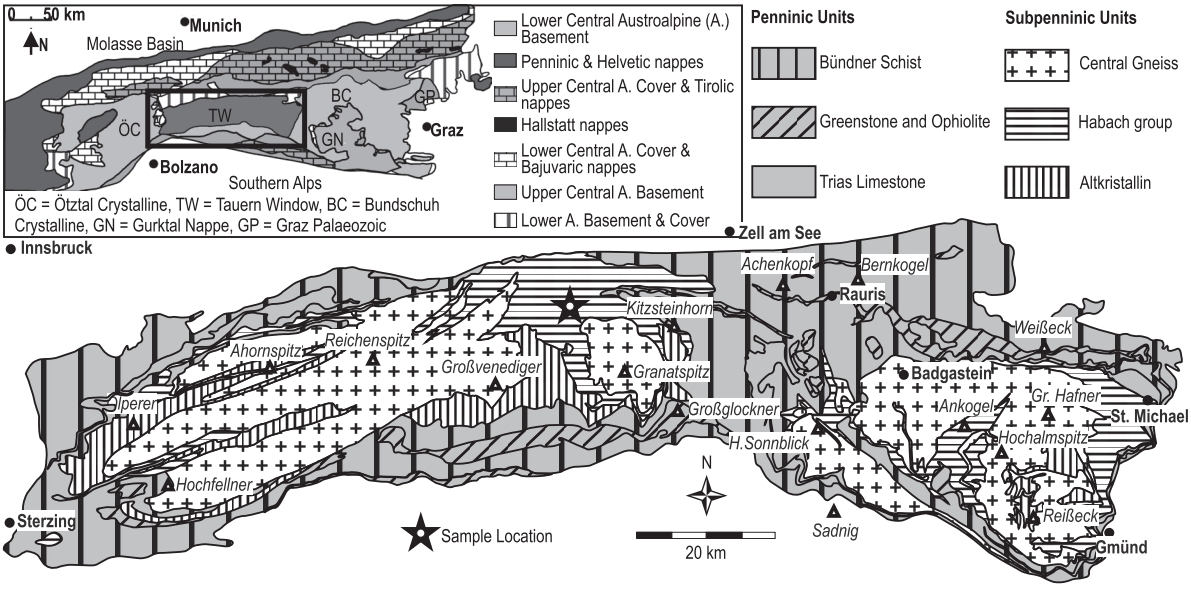

Fig. 6. Tectonic overview map of the Eastern Alps after Schmid et al. (2013) and geological map of the Tauern Window after Pestal et al. (2009).

discrete low-T events related to increased heat and fluid activity during the Permo–Triassic thinning of the European plate (Finger et al. 2017).

The K1 Gneiss, the host rock of the two complexly zoned uraninite crystals of this study, is a small orthogneiss body in the realm of the prominent scheelite mine Felbertal (47°13'27.1" N, 12°29'18.2" E; Fig. 6). It is a fine grained, SiO_2 rich, metagranitic rock (Kozlik & Raith 2016) with high concentrations of W (up to 3000 ppm), Nb (up to 100 ppm), U (up to 50 ppm) and has been regarded as the source of the local tungsten mineralization. The quartz–feldspar–mica fabric of the gneiss is entirely metamorphic (Alpidic). The magmatic protolith age of the rock has been constrained by zircon dating at 339.6±1.2 Ma (Kozlik et al. 2016).

Microstructures, EDX analyses and U–Th–total Pb ages

On average, 10–20 uraninite microcrystals are observed in a single thin section from the K1-gneiss. They are included in feldspars, epidote, titanite or zircon, only a few are interstitial. As mentioned earlier, most uraninite grains in the rock are unzoned, with a homogeneous intra-crystal U/Pb distribution that corresponds either to a Paleogene (~30 Ma) or a Permian (~265 Ma) total Pb age (Finger et al. 2017). Compositionally heterogeneous grains with internally variable U/Pb ratios and total Pb ages, as described in the following, are thus rather the exception than the rule.

Grain 1

This uraninite grain, although only some 6 µm wide, presents a striking zonation in the BSE image with a darker core and a brighter rim (Fig. 7). The boundary between the core and the rim zone is sharp, but irregularly and multiply embayed indicating replacement of older uraninite core substance by younger rim substance via coupled dissolution–reprecipitation (Putnis 2002; Harlov et al. 2011). The grain is enclosed in titanite. Other uraninite micrograins occurring nearby (Fig. 7a) are unzoned and entirely Permian in age. A small elongated fluorite crystal, recognizable by an extremely bright CL signal, adheres to grain 1 (Fig. 7c).

In order to obtain some three dimensional information, the grain surface was reground in a second step of investigation with a layer of ~0.3 µm being removed. The bright rim zone became wider (Fig. 7c), implying that larger volumes of the bright substance reside at the bottom of the grain. A narrow, ~0.2 µm wide dark chip from the older uraninite continues into the bright rim zone, documenting that coupled dissolution–reprecipitation can produce very fine-scale intracrystal heterogeneities. Such fine intergrowths are difficult to resolve and to analyse even with FE-SEM methods and naturally there is always a danger to obtain mix analyses and to calculate mix ages here.

A chemical traverse with ~0.3 µm resolution (Figs. 7b, 8a; Table 3) shows that the bright rim of grain 1 has a much lower Pb content than the core (<1 vs. ~3 wt. %), a lower Y_2O_3 content (0–2 vs. 3–4 wt %), and a higher UO_2 content (~90 vs. ~80–85 wt. %). Notably, there is no significant change in the Th content between core and rim, but the profile reveals a Th-enriched inner core within the core zone with ~10–13 wt. % ThO_2. This Th rich inner core is not very visible in the BSE image but it could be approximatively delineated by x-ray mapping. Four shorter chemical profiles were additionally recorded in different domains of grain 1 after it was reground (Figs. 7c, 8b–e, Table 3). These profiles confirm the crystallo-chemical heterogeneities within grain 1 as described before.

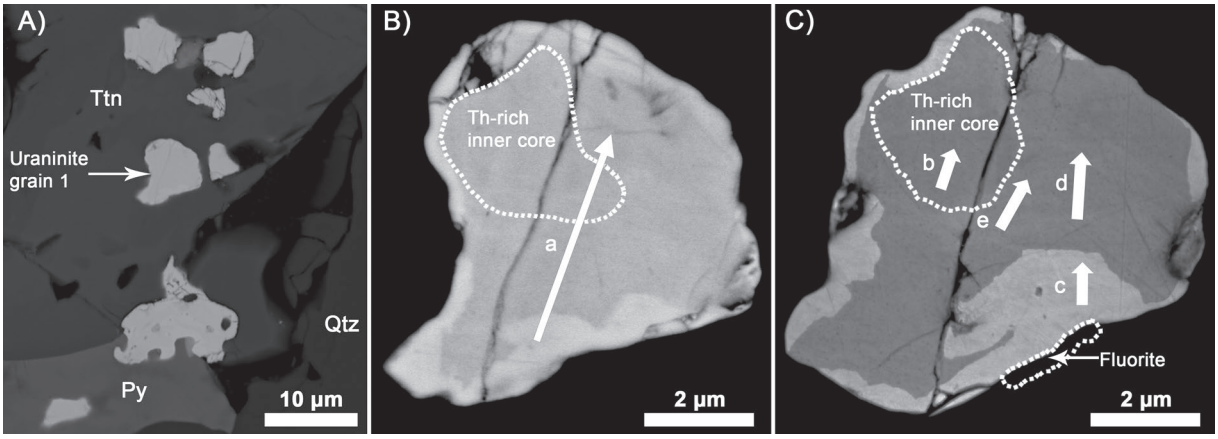

Fig. 7. BSE images for uraninite grain 1, before (**B**) and after (**C**) regrinding (see text for further information). White arrows indicate the measured chemical profiles.

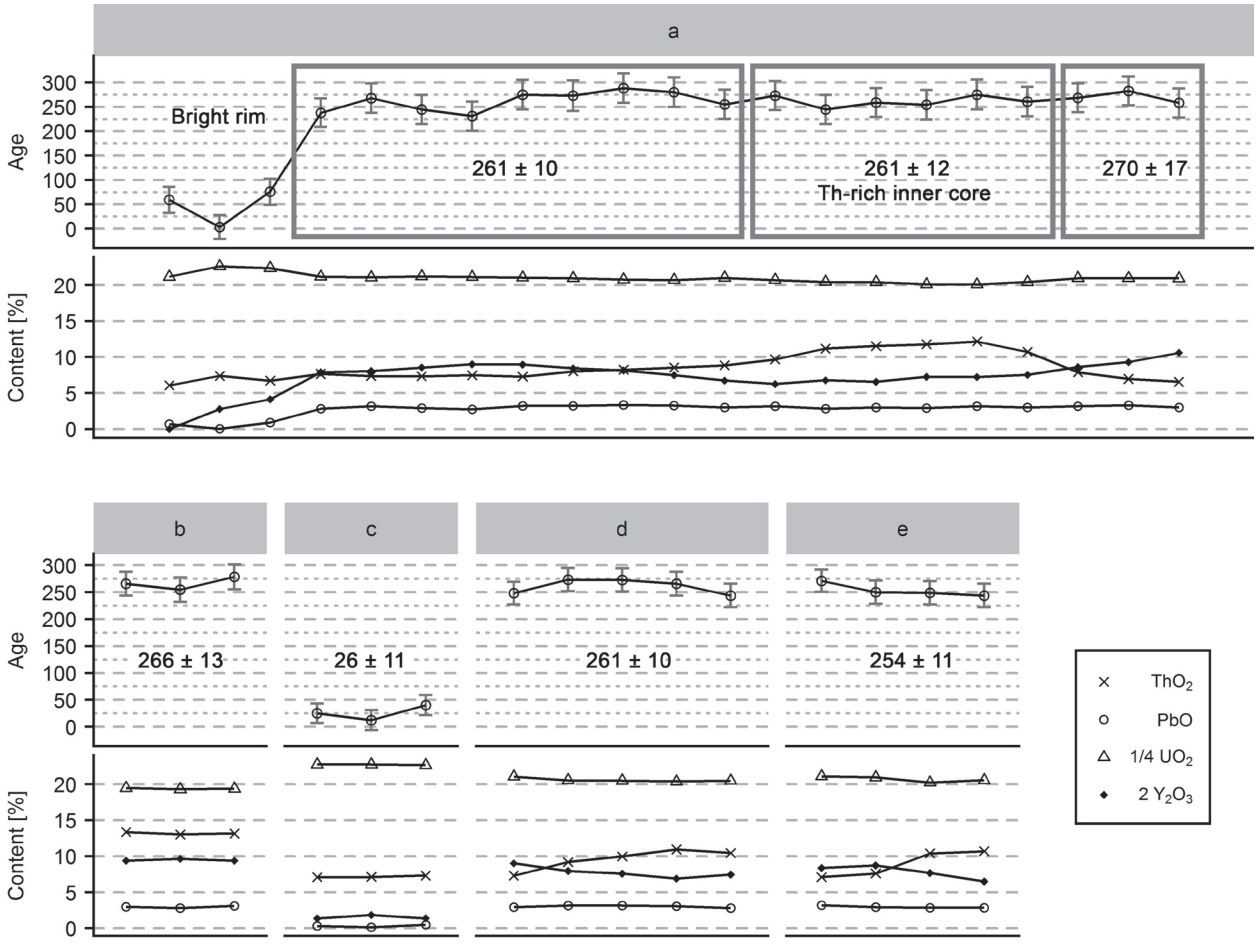

Fig. 8. Chemical profiles and total Pb ages (with 1 σ errors) recorded in grain 1. Positions of profiles are shown in Fig. 7. Given domain ages (bold) are weighted average ages (95 % confidence level).

Total Pb ages (Fig. 8, Table 3) imply that the bright uraninite rim formed during the regional metamorphic overprint of the gneiss at ~30 Ma, although the three single point ages measured in the rim sector of profile a (analyses a1–a3 in Table 3) do not give fully consistent ages. This is probably due to the presence of fine undigested remains of the precursor uraninite, which became apparent in the BSE image after regrinding (Fig. 7b and c). Profile c seems to contain lesser impurities and indicates an age of 26±11 Ma for the uraninite rim.

The total Pb ages measured in the dark core zone of grain 1 pivot around a mean of ~262 Ma. This is consistent with the Permian ages of most other uraninite grains in the rock (Finger et al. 2017). The total Pb age of the inner high-Th core falls in the same range (261±12 Ma). The core thus represents a part of the Permian growth history of the grain.

Grain 2

This relatively large subhedral uraninite grain with a size of approximately 20×40 µm is completely enclosed in epidote. Along its periphery several small fluorite crystals with bright CL signals are identified (Fig. 9a). High resolution BSE imaging (Fig. 9b and c) reveals a complex patchy zonation involving dark grey domains, medium grey domains and light grey domains. The light grey domains are typically located along the grain margin, while interior parts of the grain are middle-grey. The contacts between the middle grey central domains and the light-grey marginal domains appear rather sharp, but the BSE contrast is not very strong. Embayment textures suggest that the light-grey uraninite has replaced the middle grey uraninite via coupled dissolution–reprecipitation (Putnis 2002; Harlov et al. 2011). A thin dark grey crystal domain with elongated shape is seen in the left half of grain 2 (Fig. 9). It is sharply bordered and almost completely embedded in the middle grey substance. In the upper part of the grain in Fig 9, two puzzling small bright lenses are observed (labelled 1–2 in Fig. 9).

Several short chemical profiles were recorded in different parts of grain 2 in order to determine domain ages (Table 4). Profiles b and g are positioned in the ***dark grey domain***. Both show a relatively high Th content (~11–12 wt. % ThO_2), while U is relatively low (~80 wt. % UO_2). The higher Th/U ratios explain the darker BSE signal. The two measured domain ages are 257±7 Ma and 254±8 Ma, respectively, indicating that the dark grey zone has a Permian formation age, like most other uraninite crystals in the K1 gneiss (Finger et al. 2017).

The ***middle-grey zone*** is represented by profiles c, h and i (Figs. 9, 10). It has lower ThO_2 (~7 wt. %) and higher UO_2 (84–87 wt. %) content. The measured domain ages are 213±8, 214±7 and 200±7 Ma. The middle grey part of the crystal thus formed during the Triassic being clearly younger than the remnant dark grey domain.

The ***light grey marginal zone*** of grain 2 (profiles d and f in Figs. 9, 10) differs from the middle grey zone mainly by a lower Y content (2–2.5 vs. 2.5–3 wt. % Y_2O_3). The measured total-Pb ages are 199±9 and 208±7 Ma (Fig. 10). These age dates do not differ from those measured in the middle grey zone within the given analytical errors. Nevertheless, textures do clearly suggest that the light grey uraninite is at least slightly younger, as it has seemingly replaced the middle grey uraninite via coupled dissolution–reprecipitation.

Table 3: Chemical (wt. %) and age data for uraninite grain 1 from the Felbertal K1-gneiss (profiles a–e; see Figs. 7, 8). Single point age errors are 1 σ. Note that a shorter counting time (60 s detector live time) was used for profile a.

Grain 1 profile/point	SiO_2	CaO	Y_2O_3	PbO	ThO_2	UO_2	Total	Age [Ma]	Error (1 σ)	Live time [s]
a1	0.81	<0.27	<0.63	0.71	6.35	88.69	96.56	59	27	60
a2	0.61	<0.27	1.41	0.04	7.50	91.83	101.40	3	25	60
a3	0.73	<0.27	2.00	0.90	6.52	86.87	97.01	76	27	60
a4	0.75	<0.27	3.80	2.71	7.39	81.74	96.38	238	29	60
a5	0.52	0.46	3.83	2.99	6.99	79.99	94.78	268	30	60
a6	0.52	<0.27	4.07	2.76	6.98	80.97	95.30	245	30	60
a7	0.64	<0.27	4.30	2.60	7.16	80.95	95.65	231	30	60
a8	0.67	<0.27	4.24	3.06	6.90	79.70	94.57	275	30	60
a9	0.54	<0.27	3.89	2.96	7.41	77.44	92.23	273	31	60
a10	0.66	0.48	3.87	3.20	7.85	79.06	95.13	288	30	60
a11	0.80	0.64	3.58	3.11	8.15	79.06	95.35	280	30	60
a12	0.62	<0.27	3.21	2.87	8.43	80.18	95.31	255	30	60
a13	0.61	0.46	3.05	3.11	9.44	80.76	97.42	273	30	60
a14	0.70	<0.27	3.28	2.74	10.85	79.38	96.95	244	30	60
a15	0.51	<0.27	3.22	2.94	11.31	80.17	98.15	259	30	60
a16	0.63	0.46	3.52	2.82	11.42	78.12	96.98	254	30	60
a17	0.59	<0.27	3.50	3.05	11.76	77.75	96.65	275	30	60
a18	0.66	<0.27	3.62	2.91	10.35	78.81	96.35	261	30	60
a19	0.69	<0.27	4.43	3.45	7.82	80.29	96.68	306	30	60
a20	0.68	<0.27	4.20	3.08	7.70	81.91	97.57	269	29	60
a21	0.68	0.46	4.57	3.25	6.84	82.31	98.11	283	29	60
a22	0.70	0.55	5.14	2.92	6.36	81.27	96.94	258	30	60
						Mean	**A4-22**	**261**	**15 (2σ)**	
b1	0.61	<0.18	4.49	2.84	12.79	74.60	95.33	266	22	120
b2	0.58	0.31	4.74	2.76	12.80	75.81	97.00	255	23	120
b3	0.60	0.48	4.51	2.97	12.66	74.60	95.82	278	23	120
							Mean	**266**	**26 (2σ)**	
c1	0.46	0.46	0.66	0.30	6.91	88.71	97.50	25	18	120
c2	0.49	0.33	0.90	0.15	6.88	87.87	96.61	12	19	120
c3	0.52	0.36	0.67	0.48	7.13	88.15	97.31	40	19	120
							Mean	**26**	**21 (2σ)**	
d1	0.51	0.43	4.32	2.80	7.01	80.77	95.85	249	21	120
d2	0.59	0.47	3.87	3.08	8.95	80.09	97.05	273	22	120
d3	0.55	0.49	3.68	3.07	9.70	79.64	97.12	273	22	120
d4	0.60	0.39	3.29	2.93	10.45	77.80	95.46	266	22	120
d5	0.68	0.35	3.58	2.71	10.05	78.81	96.18	244	22	120
							Mean	**261**	**19 (2σ)**	
e1	0.59	0.49	4.05	3.09	6.86	81.61	96.69	271	21	120
e2	0.61	0.29	4.23	2.83	7.37	81.07	96.39	250	21	120
e3	0.62	0.41	3.75	2.78	10.18	79.19	96.94	249	22	120
e4	0.59	0.33	3.12	2.72	10.28	79.08	96.13	244	22	120
							Mean	**254**	**21 (2σ)**	

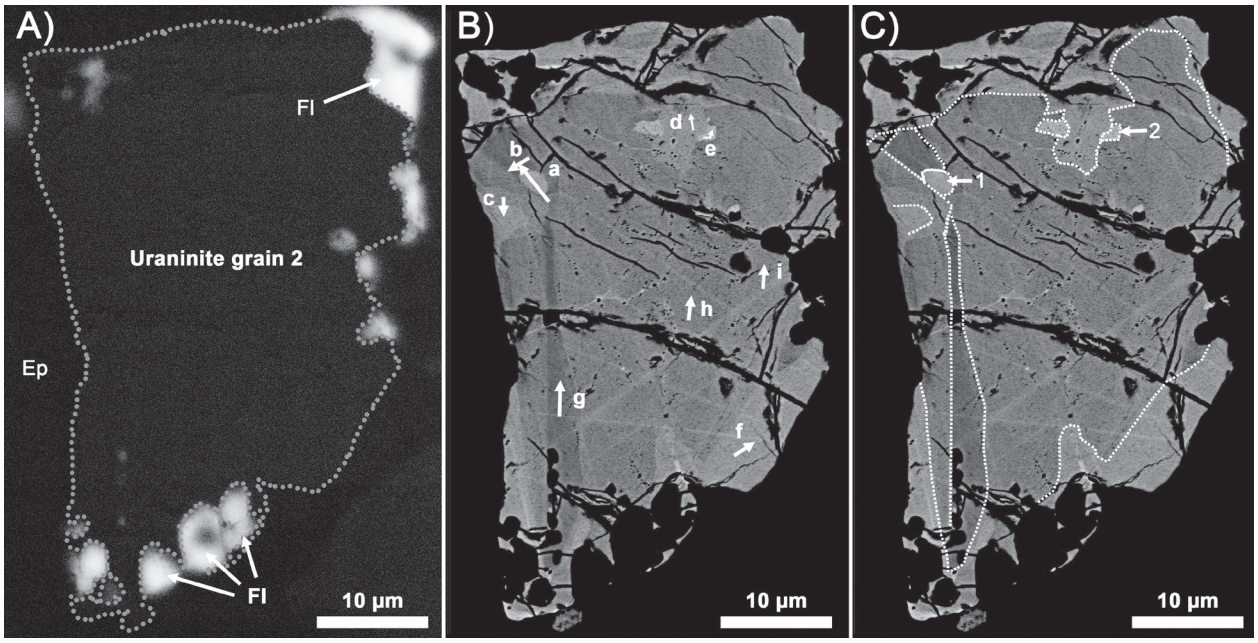

Fig. 9. CL and BSE images of grain 2. The CL image (**A**) reveals tiny fluorite crystals along the uraninite margin. The position of the measured profiles and a tentative delineation of different dissolution–reprecipitation zones in grain 2 are given in **B** and **C**.

In contrast to grain 1 we find no Paleogene rim zone in grain 2. However, one of the small bright lenses (profile a in Fig. 10) is very poor in Pb (PbO<0.5 wt. %) and thus likely represents a young regional metamorphic crystal domain. It is possible that the "lens" is, in reality, the protrusion of a larger Paleogene rim domain that is hidden underneath the crystal. Profile a shows that there was no substantial exchange of Pb between the lens and the surrounding older uraninite by solid state diffusion.

The second bright lens (profile e) is, surprisingly, of different origin. Here, the PbO contents are in the order of 2.7 wt. % corresponding to a domain age of 215±9 Ma. This lens thus formed during the Triassic, like most other parts of grain 2. Lens 2 has an unusually high UO_2 content of close to 92 wt. %, while ThO_2 (~3 wt. %), and Y_2O_3 contents (<1 wt. %) are significantly lower compared to the other parts of grain 2. The distinctive chemical composition of lens 2 and its sharp outlines would imply that practically no solid state diffusion has taken place when the whole crystal underwent reheating to ~500 °C in the Paleogene, in connection with Alpine regional metamorphism.

Discussion and conclusions

Uraninite recrystallization by coupled dissolution–reprecipitation

The two complexly zoned uraninite crystals of this study exhibit polygenetic, distinctly embayed zonation patterns, which are indicative for recrystallization by coupled dissolution–reprecipitation (Putnis 2002; Harlov et al. 2011). We have the suspicion that F-bearing fluids have caused the dissolution of the uraninite, because both recrystallized uraninite grains are bordered by small fluorite crystals. The important role of F for the solubility of U in melts and fluids has been pointed out many times (Keppler & Whyllie 1990; Peiffert et al. 1996).

We would argue that, in our case, the process of uraninite recrystallization by coupled dissolution–reprecipitation involved only small local fluid volumes, because in the presence of larger volumes of U-undersaturated fluids, the dissolved U would have been most likely transported away and not reprecipitated at the spot.

The fact that dissolution–reprecipitation driven recrystallization of uraninite obviously can happen a couple of times during the geological evolution of a rock, is extremely fortunate for the field of geochronology. Multiply recrystallized uraninite can be viewed as a sensitive "hard disk" where several geological events of an area are stored. Most importantly, this "uraninite hard disc" may include information of discrete low-T events that are commonly not recorded by other geochronometers (Finger et al. 2017).

Geochronological robustness of uraninite

In-situ chemical dating of uraninite by means of electron beam excitation and X-ray spectroscopy is not new (Parslow et al. 1985; Bowles 1990). It was successfully used before chemical U–Th–Pb dating of monazite started, but was never widely applied. The method remained restricted to studies of uraninite and pitchblende in U deposits (Alexandre & Kyser 2005; Cross et al. 2011; Shahin 2014; Ge et al. 2014) and to accessory magmatic uraninite in granitic rocks (Förster 1999;

Table 4: Chemical (wt. %) and age data for uraninite grain 2 from the Felbertal K1 gneiss (profiles a–i; see Figs. 9 and 10). Single point age errors are 1 σ. Note that a shorter counting time (60 s detector live time) was used for profile a.

Grain 2 profile/point	SiO_2	CaO	Y_2O_3	PbO	ThO_2	UO_2	Total	Age [Ma]	Error (1 σ)	Live time [s]
a1	0.31	0.41	2.53	2.71	10.03	81.70	97.69	236	29	60
a2	0.49	0.47	2.66	2.72	8.47	83.41	98.22	234	30	60
a3	0.46	0.40	3.20	2.64	10.72	79.98	97.40	234	31	60
a4	0.40	<0.27	2.71	0.62	11.43	81.20	96.35	55	28	60
a5	0.47	<0.27	2.58	0.38	10.12	84.60	98.15	32	27	60
a6	0.51	<0.27	2.38	0.24	9.49	83.95	96.57	21	28	60
a7	0.43	<0.27	2.29	0.36	10.09	84.59	97.76	31	27	60
a8	0.38	<0.27	2.27	0.30	10.26	85.42	98.63	26	27	60
a9	0.43	<0.27	2.20	0.45	9.94	85.71	98.74	38	27	60
a10	0.34	<0.27	2.18	0.33	10.76	84.06	97.67	29	27	60
a11	0.55	<0.27	2.75	0.15	9.40	84.90	97.74	12	27	60
a12	0.34	<0.27	2.38	0.28	9.52	84.94	97.46	24	27	60
a13	0.53	<0.27	2.61	0.61	9.68	85.16	98.58	52	27	60
a14	0.45	<0.27	3.19	1.17	11.43	80.88	97.12	104	29	60
a15	0.48	0.48	3.25	2.57	11.17	79.39	97.33	229	31	60
a16	0.48	0.49	3.32	2.73	11.39	78.01	96.42	247	32	60
a17	0.42	0.50	3.36	3.01	11.60	78.50	97.40	269	32	60
b1	0.48	0.53	3.07	2.94	10.95	80.72	98.69	257	21	120
b2	0.47	0.51	2.97	2.95	11.36	80.26	98.51	259	22	120
b3	0.60	0.51	3.00	3.00	11.30	79.53	97.94	266	22	120
b4	0.76	0.53	3.33	2.92	11.31	78.13	96.98	263	23	120
b5	0.84	0.38	3.29	2.94	11.57	78.63	97.65	263	22	120
b6	0.86	0.32	3.44	2.74	11.48	78.64	97.48	246	22	120
b7	0.67	0.49	3.12	2.89	11.48	79.33	97.98	257	22	120
b8	0.77	0.53	3.38	2.82	11.56	78.04	97.11	255	23	120
b9	0.75	0.63	3.07	2.75	11.55	79.54	98.29	244	22	120
b10	0.75	0.57	3.43	2.89	11.76	78.16	97.57	260	23	120
							Mean	**257**	**14 (2σ)**	
c1	0.52	<0.18	3.18	2.72	8.40	84.39	99.21	231	21	120
c2	0.73	<0.18	3.20	2.44	8.27	82.91	97.56	211	21	120
c3	0.75	<0.18	3.37	2.36	7.87	83.41	97.76	204	21	120
c4	0.73	<0.18	2.37	2.65	6.86	85.76	98.36	222	20	120
c5	0.71	<0.18	2.32	2.50	6.50	86.33	98.37	210	20	120
c6	0.70	<0.18	2.29	2.41	6.37	86.62	98.39	201	20	120
							Mean	**213**	**16 (2σ)**	
d1	0.43	<0.18	2.32	2.30	8.47	85.05	98.57	194	19	120
d2	0.48	0.24	2.07	2.39	8.62	83.70	97.51	205	20	120
d3	0.47	<0.18	2.21	2.50	8.19	83.31	96.70	216	20	120
d4	0.55	<0.18	2.44	2.19	8.31	82.90	96.39	190	20	120
d5	0.44	0.25	2.32	2.22	8.14	84.44	97.80	189	20	120
							Mean	**199**	**18 (2σ)**	
e1	0.34	<0.18	<0.39	2.63	3.10	92.62	98.69	208	18	120
e2	0.36	<0.18	0.54	2.71	3.49	92.57	99.66	214	18	120
e3	0.41	0.34	0.59	2.81	2.85	91.78	98.77	224	19	120
							Mean	**215**	**21 (2σ)**	
f1	0.44	<0.18	2.32	2.34	7.22	85.46	97.79	198	19	120
f2	0.43	<0.18	2.18	2.61	7.47	84.75	97.44	221	20	120
f3	0.45	<0.18	2.46	2.72	7.53	85.27	98.42	229	20	120
f4	0.39	0.26	2.14	2.39	7.44	85.09	97.71	202	20	120
f5	0.42	<0.18	2.26	2.52	7.17	84.56	96.93	215	20	120
f6	0.41	0.30	2.13	2.29	7.74	85.18	98.05	194	20	120
f7	0.45	0.25	2.39	2.34	7.19	84.81	97.43	199	20	120
f8	0.49	<0.18	2.46	2.52	7.19	84.71	97.37	214	20	120
f9	0.40	<0.18	2.16	2.35	7.62	85.57	98.10	198	20	120
							Mean	**208**	**13 (2σ)**	
g1	0.47	0.52	3.20	2.93	11.76	79.85	98.73	258	21	120
g2	0.44	0.64	3.16	2.72	11.73	78.29	96.99	245	22	120
g3	0.56	0.50	3.25	2.67	11.62	77.42	96.01	243	22	120
g4	0.42	0.49	2.99	2.91	12.01	78.11	96.93	261	22	120
g5	0.51	0.56	3.22	3.12	11.72	77.56	96.69	282	22	120
g6	0.55	0.52	3.07	2.70	11.79	77.99	96.61	244	22	120
g7	0.53	0.55	3.11	2.70	11.95	78.65	97.49	242	23	120
g8	0.56	0.35	3.19	2.81	11.71	78.16	96.79	253	22	120
							Mean	**254**	**16 (2σ)**	
h1	0.44	0.55	2.62	2.56	7.12	84.07	97.37	219	20	120
h2	0.38	0.63	2.59	2.70	7.32	84.20	97.80	230	21	120
h3	0.46	0.43	2.77	2.56	7.04	85.67	98.92	216	20	120
h4	0.47	0.54	2.64	2.75	7.12	84.41	97.92	235	21	120
h5	0.46	0.66	2.55	2.44	7.47	84.63	98.21	208	21	120
h6	0.50	0.52	2.78	2.38	7.00	84.38	97.56	204	21	120
h7	0.50	0.44	2.57	2.44	7.11	84.59	97.65	208	21	120
h8	0.54	0.79	2.81	2.30	7.22	85.26	98.91	194	21	120
h9	0.44	0.55	2.62	2.56	7.12	84.07	97.37	219	20	120
							Mean	**214**	**14 (2σ)**	
i1	0.50	0.49	2.73	2.40	6.92	85.38	98.41	203	20	120
i2	0.41	0.57	2.67	2.24	7.38	85.83	99.11	188	20	120
i3	0.51	0.42	2.83	2.53	6.79	84.39	97.48	217	21	120
i4	0.50	0.47	2.70	2.59	7.22	85.75	99.24	218	20	120
i5	0.49	0.39	2.76	2.37	6.97	87.02	99.99	196	20	120
i6	0.53	0.39	2.79	2.26	6.91	85.45	98.34	191	21	120
i7	0.54	0.66	2.79	2.26	6.87	85.58	98.70	191	20	120
							Mean	**215**	**15 (2σ)**	

Kempe 2003; Hurtado et al. 2007; Cocherie & Legende 2007; Votyakov et al. 2013).

A more widespread application would result from the study of uraninite microcrystals in metamorphic rocks. The increasing use of electron microscopy in petrographic studies shows that uraninite microcrystals occur in many metamorphic rocks. The potential of uraninite dating in metamorphic terranes will greatly depend on the geochronological robustness of the U–Th–Pb system in the mineral. We present here unequivocal evidence that even very small uraninite crystals can survive an amphibolite facies overprint, preserving domains with intact U–Th–Pb ratios. It must be taken into account, though, that different age domains in polygenetic uraninite can be so small and intimately intergrown with each other that they are very difficult to resolve and to analyse. Dating results can be problematic in such cases. The risk of Pb loss through solid state diffusion is low for unaltered uraninite at low to medium temperatures. However, fine scale uraninite alteration to U silicate (coffinite) and other secondary U minerals may cause Pb loss (Kempe 2003). It is therefore imperative that uraninite age data is always collected in combination with detailed backscatter electron imagery and high-resolution compositional profiles across single grains.

U–Th–Pb geochronometry with submicron-scale resolution and the potential of the SEM/EDX method

It is obvious that the geochronological investigation of micron-sized zoning patterns in uraninite microcrystals requires an analytical resolution much finer than what is presently possible with Laser-ICP-MS methods (typically 15–30 µm spots), and even with the latest and best SHRIMPs (around 5–10 µm spot resolution). Among all the currently available isotopic analytical methods, only the SIMS technique possesses the required spatial

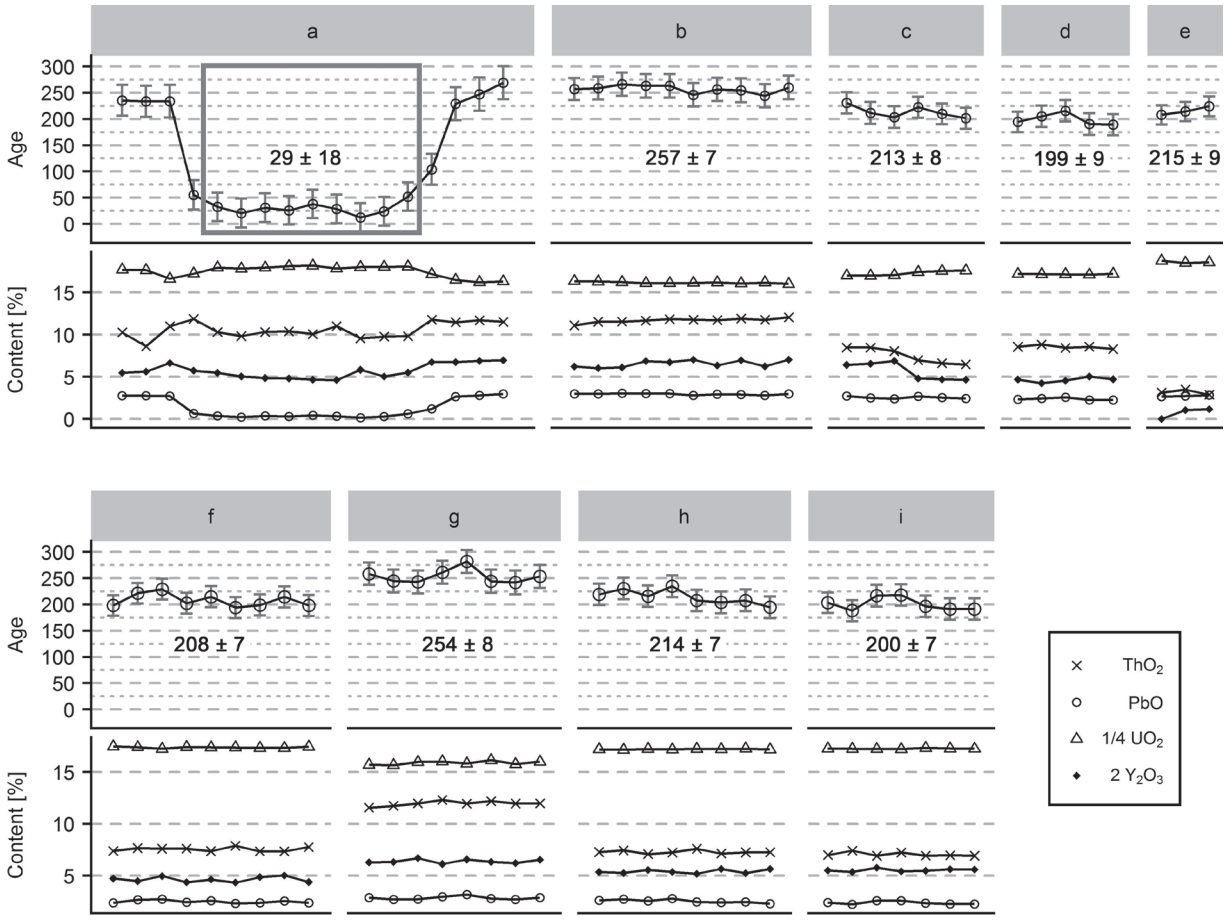

Fig. 10. Chemical profiles and total Pb ages recorded in grain 2 (positions of profiles are shown in Fig. 9). Shown error bars are 1 σ. Given domain ages (bold) are weighted average ages (95 % confidence level).

resolution to analyse micron-sized crystal domains. The Cameca nano-SIMS, for instance, allegedly can achieve a spatial resolution of 50 nm (Kilburn & Wacey 2014). However, practical applications of Th–U–Pb dating with nano-SIMS measurements have not yet been made with spot sizes <2–3 µm (Fayek et al. 2002; Stern et al. 2005; Koike et al. 2014) as it is methodically difficult, even with the latest nano-SIMS devices. Thus, there appears to be currently no real alternative to electron beam dating on such small scales.

So far, the ~1 µm spot size obtained by electron microprobe-based dating in the classical 15 kV set-up was the lower limit for quantitative Th–U–Pb geochronometry. In this study, we have applied for the first time finer-scale total Pb dating on the submicron level by means of low-voltage SEM/EDX techniques. We have used so-called standardless EDX analysis for uraninite dating. This method relies on factory-based intensity ratios (counts per wt. %) that were initially measured for all elements at 20 kV on appropriate element standards (see Table 1). Therefore, the term "standardless" may be somewhat misleading. These intensity values must be "updated" before every analytical session by means of a monitor standard. We did this by measuring Si count rates and background signals on a silicon wafer.

We know that EDX analysis, especially when run in standardless mode, is viewed by many workers in the field with scepticism with regard to whether it can provide sufficient precision and accuracy for U–Th–total Pb dating. The main problems are that the factory-based intensity values need to be extrapolated to other beam conditions (in our case, 8 kV) by using fundamental parameters, and that intensity ratios between elements may change when the instrument ages. However, based on systematic measurements on a number of reference materials, we propose here that standardless SEM/EDX analyses with the Oxford INCAEnergy system can provide geologically meaningful uraninite ages with a reasonable precision and accuracy. The correctness of the primary standardization can easily be tested by means of control measurements on synthetic UO_2 and ThO_2 and other element standards. If these standards give systematically to high or too low values, this could be reasonably considered with a later external correction and recalibration. A certain analytical problem could result from the fact that Th Mα and U Mα lines overlap in the EDX spectrum (Fig. 2). This involves the risk of an inaccurate U and Th determination in Th rich uraninite. However, as mentioned earlier, slight errors in the U and Th contents will have little effect on the age dates.

By far the most important factor for successful U–Th–total Pb uraninite dating is certainly the accuracy of the Pb determination. Fortunately, the latter can be sensitively controlled with uraninite reference materials, but a variety of such "age standards" with different compositions is needed to minimize the risk of systematic errors caused by inaccurate peak interference or the background correction. A minor systematic error in the age, on the order of a few million years, may still remain unrecognized though, due to the limited precision of EDX analysis. Either way, the EDX data quality appears to be definitely sufficient to study essential features of uraninite recrystallization and alteration. The special construction of scanning electron microscopes, directed towards a particularly high beam stability, is advantageous for high spatial resolution measurements, as is the ability of EDX detectors to analyse all elements simultaneously.

A severe limitation of our analytical setup and of the EDX method, in general, concerns the dating of very young uraninite (<20 Ma), where radiogenic Pb is close to or even remains below the detection limit. WDX analysis would certainly have more potential here. Moreover, WDX analysis could provide superior precision for U–Th–total Pb uraninite dating. It seems possible that, with a good WDX setup, uraninite spot analyses can be made with errors of less than 1 million years. This would theoretically permit high-precision dating of uraninite. However, due to the danger of small-scale intra-crystal age heterogeneities, such application would only make sense in combination with a high spatial analytical resolution and a very high beam stability, respectively. Whether electron microprobes can achieve equally good beam stability behaviour as the state-of-the-art FE-SEMs still needs to be tested.

Acknowledgements: Noreen Vielreicher is thanked for stylistic and linguistic improvements of the text. Hans-Jürgen Förster, Axel Renno and Olaf Tietz donated hand specimens of uraninite bearing granite types from the Erzgebirge, which served as valuable uraninite "age standards". Reinhard Wagner and Werner Paar provided uraninite crystals from the Mitterberg ore deposit. Funding in the frame of the program "Forschungspartnerschaften Mineralrohstoffe" of the Austrian Geological Survey (GBA) and by the Austrian Science Fund (P 31901-N29) is gratefully acknowledged. The paper benefited from competent reviews by Daniel Harlov, Bernhard Schulz and Armin Zeh.

References

Allaz J., Raschke M.B., Persson Ph.M. & Stern Ch.R. 2015: Age, petrochemistry, and origin of a REE-rich mineralization in the Longs Peak–St. Vrain batholith, near Jamestown, Colorado (U.S.A.). *Am. Mineral.* 100, 2123–2140.

Alexandre P. & Kyser T.K. 2005: Effects of cationic substitutions and alteration in uraninite, and implications for the dating of uranium deposits. *Can. Mineral.* 43, 3, 1005–1017.

Alexandre P., Peterson R. & Joy B. 2016: Sector Zoning In Uraninite. *Can. Mineral.* 53, 1–11.

Amelin Y. & Davis W.J. 2006: Isotopic analysis of lead in sub-nanogram quantities by TIMS using a ^{202}Pb–^{205}Pb spike. *J. Anal. At. Spectrom.* 21, 10, 1053–1061.

Bernhard F., Finger F., Schitter F., Berka R. & Schuster R. 1998: Electron microprobe ages of monazite and xenotime from the Austroalpine basement units of the Fischbacher Alpen, Styria, Austria. *Mitt. Österreich. Mineral. Gesellschaft* 143, 246–248.

Bowles J.F.W. 1990: Age dating of individual grains of uraninite in rocks from electron microprobe analyses. *Chem. Geol.* 83, 1–2, 47–53.

Chipley D., Polito P.A. & Kyser T.K. 2007: Measurement of U–Pb ages of uraninite and davidite by laser ablation-HR-ICP-MS. *Am. Mineral.* 92, 11–12, 1925–1935.

Cliff R.A., Oberli F., Meier M., Droop G.T.R. & Kelly M. 2015: Syn-metamorphic folding in the Tauern Window, Austria dated by Th–Pb ages from individual allanite porphyroblasts. *J. Metamorph. Geol.* 33, 4, 427–435.

Cocherie A. & Legendre O. 2007: Potential minerals for determining U–Th–Pb chemical age using electron microprobe. *Lithos* 93, 3–4, 288–309.

Cross A., Jaireth S., Rapp R. & Armstrong R. 2011: Reconnaissance-style EPMA chemical U–Th–Pb dating of uraninite. *Australian J. Earth Sci.* 58, 6, 675–683.

Davis D.W., Krogh T.E. & Williams I.S. 2003: Historical Development of Zircon Geochronology. *Rev. Mineral. Geochem.* 53, 1, 145–181.

Decrée S., Deloule E., Putter T., Dewaele S., Mees F., Yans J. & Marignac C. 2011: SIMS U–Pb dating of uranium mineralization in the Katanga Copperbelt: Constraints for the geodynamic context. *Ore Geol. Rev.* 40, 1, 81–89.

Drouin D., Couture A.R., Joly D., Tastet X., Aimez V. & Gauvin R. 2007: "CASINO V2.42" — A fast and easy-to-use modeling tool for scanning electron microscopy and microanalysis users. *Scanning* 29, 92–101.

Eichhorn R., Loth G., Höll R., Finger F., Schermaier A. & Kennedy A. 2000: Multistage Variscan magmatism in the central Tauern Window (Austria) unveiled by U/Pb SHRIMP zircon data. *Contrib. Mineral. Petrol.* 139, 4, 418–435.

Eichhorn R., Schärer U. & Höll R. 1995: Age and evolution of scheelite-hosting rocks in the Felbertal deposit (Eastern Alps): U–Pb geochronology of zircon and titanite. *Contrib. Mineral. Petrol.* 119, 4, 377–386.

Fayek M., Kyser T.K. & Riciputi L.R. 2002: U and Pb Isotpe analysis of uranium minerals by ion microprobe and the geochronology of the McArthur River and Sue Zone uranium deposits, Saskatchewan, Canada. *Can. Mineral.* 40, 6, 1553–1570.

Finger F., Krenn E., Schulz B., Harlov D. & Schiller D. 2016: "Satellite monazites" in polymetamorphic basement rocks of the Alps: Their origin and petrological significance. *Am. Mineral.* 101, 5, 1094.

Finger F., Waitzinger M., Förster H.J., Kozlik M. & Raith J. 2017: Identification of discrete hydrothermal events in polymetamorphic basement rocks using high spatial resolution U–Th–Pb chemical dating of uraninite microcrystals. *Geology* 45, 991–994.

Förster H.J. 1999: The Chemical Composition of Uraninite in Variscan Granites of the Erzgebirge, Germany. *Mineral. Mag.* 63, 2, 239–252.

Förster H.J., Rhede D., Stein H.J., Romer R.L. & Tischendorf G. 2012: Paired uraninite and molybdenite dating of the Königshain granite: implications for the onset of late-Variscan magmatism in the Lausitz Block. *Int. J. Earth Sci. (Geol. Rundsch.)* 101, 57–67.

Frasl G. & Frank W. 1966: Einführung in die Geologie und Petrographie des Penninikums im Tauernfenster. *Der Aufschluß*, Spec. Issue 15, Heidelberg, 30–58.

Frei D. & Gerdes A. 2009: Precise and accurate in situ U–Pb dating of zircon with high sample throughput by automated LA-SF-ICP-MS. *Chem. Geol.* 261, 3–4, 261–270.

Ge X., Qin M. & Fan G. 2014: Study and Application of Electron Probe Micro-analysis Dating for Uraninite. *Acta Geologica Sinica — English Edition* 88, s2, 1345–1346.

Geisler T. & Schleicher H. 2000: Improved U–Th–total Pb dating of zircons by electron microprobe using a simple new background modeling procedure and Ca as a chemical criterion of fluid-induced U–Th–Pb discordance in zircon. *Chem. Geol.* 163, 1–4, 269–285.

Harlov D.E., Wirth R. & Hetherington C.J. 2011: Fluid-mediated partial alteration of monazite: the role of coupled dissolution–reprecipitation in element redistribution and mass transfer. *Contrib. Mineral. Petrol.* 162, 329–348.

Holmes A. 1911: The Association of Lead with Uranium in Rock-Minerals, and Its Application to the Measurement of Geological Time. *Proceedings of the Royal Society of London A: Mathematical, Physical and Engineering Sciences* 85, 578, 248–256.

Hurtado J.M., Chatterjee N., Ramezani J., Hodges K.V. & Bowring S.A. 2007: Electron Microprobe Chemical Dating of Uraninite as a Reconnaissance Tool for Leucogranite Geochronology. *Nature Precedings*, hdl:10101/npre.2007.655.1.

Jercinovic M.J. & Williams M.L. 2005: Analytical perils (and progress) in electron microprobe trace element analysis applied to geochronology: background acquisition, interferences, and beam irradiation effects. *Am. Mineral.* 90, 526–546.

Jercinovic M.J., Williams M.L., Allaz J. & Donovan J. 2012: Trace Analysis in EPMA. *IOP Conf. Series: Materials Science and Engineering* 32, 1–22.

Kebede T., Klotzli U., Kosler J. & Torbjorn S. 2005: Understanding the pre-Variscan and Variscan basement components of the central Tauern Window, Eastern Alps (Austria): constraints from single zircon U–Pb geochronology. *Int. J. Earth Sci.* 94, 336–353.

Keppler H. & Whyllie P.J. 1990: Role of fluids in transport and fractionation of uranium and thorium in magmatic processes. *Nature* 348, 531–533.

Kempe U. 2003: Precise electron microprobe age determination in altered uraninite: consequences on the intrusion age and the metallogenic significance of the Kirchberg granite (Erzgebirge, Germany). *Contrib. Mineral. Petrol.* 145, 1, 107–118.

Kober B. 1986: Whole-grain evaporation for $^{207}Pb/^{206}Pb$-age-investigations on single zircons using a double-filament thermal ion source. *Contrib. Mineral. Petrol.* 93, 4, 482–490.

Kilburn M.R. & Wacey D. 2014: Nanoscale secondary ion mass spectrometry (NanoSIMS) as an analytical tool in the geosciences. In: Grice K (Ed.): Principles and Practice of Analytical Techniques in Geosciences. *The Royal Society of Chemistry*, 1–34.

Koike M., Ota Y., Sano Y., Takahata N. & Sugiura N. 2014: High-spatial resolution U–Pb dating of phosphate minerals in Martian meteorite Allan Hills 84001. *Geochem. J.* 48, 5, 423–431.

Kotzer T.G. & Kyser T.K. 1993: O, U, and Pb isotopic and chemical variations in uraninite; implications for determining the temporal and fluid history of ancient terrains. *Am. Mineral.* 78, 11–12, 1262–1274.

Kozlik M. & Raith J. 2016: Variscan metagranitoids in the central Tauern Window (Eastern Alps, Austria) and their role in the formation of the Felbertal scheelite deposit. *Lithos* 278, 303–320.

Kozlik M., Raith J.G. & Gerdes A. 2016: U–Pb, Lu–Hf and trace element characteristics of zircon from the Felbertal scheelite deposit (Austria): New constraints on timing and source of W mineralization. *Chem. Geol.* 421, 112–126.

Krogh T.E. 1982: Improved accuracy of U-Pb zircon ages by the creation of more concordant systems using an air abrasion technique. *Geochim. Cosmochim. Acta* 46, 4, 637–649.

Ludwig K.R. 2003: User's manual for Isoplot 3.00: a geochronological toolkit for Microsoft Excel. *Kenneth R. Ludwig,* 1–74.

Mattinson J.M. 2005: Zircon U–Pb chemical abrasion ("CA-TIMS") method: Combined annealing and multi-step partial dissolution analysis for improved precision and accuracy of zircon ages. *Chem. Geol.* 220, 1–2, 47–66.

Montel J.-M., Foret S., Veschambre M., Nicollet C. & Provost A. 1996: Electron microprobe dating of monazite. *Chem. Geol.* 131, 1, 37–53.

Montel J.M., Kato T., Enami M., Cocherie A., Finger F., Williams M. & Jercinovic M. 2017: Electron probe dating of monazite — the story. *Chem. Geol.* 484, 4–15.

Naemura K., Hirajima T. & Svojtka M. 2009: The Pressure–Temperature Path and the Origin of Phlogopite in Spinel–Garnet Peridotites from the Blanský Les Massif of the Moldanubian Zone, Czech Republic. *J. Petrol.* 50, 10, 1795–1827.

Paar W. & Koeppel V. 1978: The 'pitchblende-nodule-assemblage' of Mitterberg (Salzburg, Austria). *Neues Jahrb. Mineral. Abh.* 131, 3, 254–271.

Parslow G.R., Bandstaetter F., Kurat G. & Thomas D.J. 1985: Chemical ages and mobility of U and Th in anatectites of the Cree Lake zone, Saskatchewan. *Can. Mineral.* 23, 4, 543–551.

Pestal G., Hejl E., Braunstingl R. & Schuster R. 2009: Erläuterungen Geologische Karte von Salzburg 1:200,000. *Geologische Bundesanstalt*, Wien, 1–162.

Peiffert C., Nguyen Trung C. & Cuney M. 1996: Uranium in granitic magmas. Part II: experimental determination of uranium solubility and fluid-melt partition coefficients in the UO_2-haplogranite-H_2O-halides system at 720-770°C, 200 MPa. *Geochim. Cosmochim. Acta* 60, 1515–1529.

Putnis A. 2002: Mineral replacement reactions: from macroscopic observations to microscopic mechanisms. *Mineral. Mag.* 66, 689–708.

Pyle J.M., Spear F.S. & Wark D.A. 2002: Electron Microprobe Analysis of REE in Apatite, Monazite and Xenotime: Protocols and Pitfalls. Rev. Mineral. Geochem. 48, 1, 337–362.

Săbău G. 2012: Chemical U–Th–Pb geochronology: a precise explicit approximation of the age equation and associated errors. *Geochronometria* 39, 167 –179.

Santosh M., Yokoyama K., Biju-Sekhar S. & Rogers J.J.W. 2003: Multiple Tectonothermal Events in the Granulite Blocks of Southern India Revealed from EPMA Dating: Implications on the History of Supercontinents. *Gondwana Res.* 6, 1, 29–63.

Schaltegger U., Schmitt A.K. & Horstwood M.S.A. 2015: U–Th–Pb zircon geochronology by ID-TIMS, SIMS, and laser ablation ICP-MS: Recipes, interpretations, and opportunities. *Chem. Geol.* 402, 89–110.

Scherrer N., Engi M., Gnos E., Jakob V. & Liechti A. 2000: Monazite analysis; from sample preparation to microprobe age dating and REE quantification. *Schweiz. Mineralog. Petrograph. Mitt*. 80, 1, 93–105.

Schmid S.M., Fügenschuh B., Kissling E. & Schuster R. 2004: Tectonic map and overall architecture of the Alpine orogen. *Eclogae Geologicae Helvetiae* 97, 1, 93–117.

Schmid S.M., Scharf A., Handy M.R. & Rosenberg C.L. 2013: The Tauern Window (Eastern Alps, Austria): a new tectonic map, with cross-sections and a tectonometamorphic synthesis. *Swiss J. Geosci.* 106, 1, 1–32.

Schoene B., Guex J., Bartolini A., Schaltegger U. & Blackburn T.J. 2010: Correlating the end-Triassic mass extinction and flood basalt volcanism at the 100 ka level. *Geology* 38, 5, 387–390.

Shahin H.A. 2014: Geochemical Characteristics and Chemical Electron Microprobe U–Pb–Th Dating of Pitchblende Mineralization from Gabal Gattar Younger Granite, North Eastern Desert, Egypt. *Open Journal of Geology* 4, 24–32.

Stern R.A., Fletcher I.R., Rasmussen B., McNaughton N.J. & Griffin B.J. 2005: Ion microprobe (NanoSIMS 50) Pb-isotope geochronology at <5 μm scale. *Int. J. Mass Spectrom.* 244, 2–3, 125–134.

Suzuki K., Adachi M. & Tanaka T. 1991: Middle precambrian provenance of Jurassic sandstone in the Mino Terrane, central Japan: Th–U-total Pb evidence from an electron microprobe monazite study. *Sediment. Geol.* 75, 1–2, 141–147.

Tropper P., Harlov D., Krenn E., Finger F., Rhede D. & Bernhard F. 2007: Zr-bearing minerals as indicators for the polymetamorphic evolution of the eastern, lower Austroalpine nappes (Stubenberg Granite contact aureole, Styria, Eastern Alps, Austria). *Lithos* 95, 1–2, 72–86.

Vesela P., Soellner F., Finger F. & Gerdes A. 2012: Magmato–sedimentary Carboniferous to Jurassic evolution of the western Tauern window, Eastern Alps (constraints from U–Pb zircon dating and geochemistry) (vol. 100, pg. 993, 2011). *Int. J. Earth Sci.* 101, 2, 603.

von Quadt A. 1992: U–Pb zircon and Sm–Nd geochronology of mafic and ultramafic rocks from the central part of the Tauern Window (eastern Alps). *Contrib. Mineral. Petrol.* 110, 1, 57–67.

Votyakov S.L., Khiller V.V., Shchapova Y.V. & Erokhin Y.V. 2013: Composition and chemical microprobe dating of U–Th-Bearing minerals. Part 2. Uraninite, thorite, thorianite, coffinite, and monazite from the Urals and Siberia. *Geol. Ore Deposits* 55, 7, 515–524.

Williams I.S. 1998: U–Th–Pb geochronology by ion microprobe. In: McKibben M.A., Shanks W.C., Ridley W.I. (Eds.): Applications of Microanalytical Techniques to Understanding Mineralizing Processes. *Reviews in Economic Geology*, Littleton, 1–35.

Williams M.L. & Jercinovic M.J. 2002: Microprobe monazite geochronology: putting absolute time into microstructural analysis. *J. Struct. Geol.* 24, 6–7, 1013–1028.

Yokoyama K., Shigeoka M., Goto A., Terada K., Hidaka H. & Tsutsumi Y. 2010: U–Th-total Pb ages of Uraninite and Thorite from Granititc Rocks in the Japanese Islands. *Bull. Natl. Mus. Nat. Sci.* 36, 7–18.